Critical Temperature for Superconductivity Phase Transition in $Ba(Fe_{1-x}Co_x)_2As_2$*

Yiming Teng,† Derap Pena Mukti Sari,‡ and Xingyu Chen§
Université Paris-Saclay
(Dated: June 13, 2025)

We examine the superconducting transition in $Ba(Fe_{1-x}Co_x)_2As_2$ using precision cryogenic techniques and resistance measurements. The resistance-temperature data from two samples revealed the characteristic resistance drop of the superconducting phase transition, with critical temperatures determined as $T_{c,1} = 20.15$ K and $T_{c,2} = 15.83$ K. Doping concentrations were constrained to $x_1 = 0.056$ or 0.082 and $x_2 = 0.048$ or 0.101. Despite limitations including equipment malfunction and incomplete data, this experiment offers us a deeper understanding of cryogenic methodologies and superconductivity in iron-based materials.

I. INTRODUCTION

Superconductivity, the phenomenon that certain materials exhibit zero electrical resistance and expulsion of magnetic fields below a critical temperature has been a fascinating topic in physics since its discovery.

The journey of superconductivity began in 1911 when Dutch physicist Heike Kamerlingh Onnes discovered the phenomenon while studying the electrical resistance of mercury at extremely low temperatures. Using liquid helium to cool mercury, he observed that its resistance disappeared entirely at 4.2 K, which marked the birth of superconductivity. Twenty-four years later, Brothers Fritz and Heinz London proposed phenomenological equations to describe the exotic electromagnetic properties of superconductors, known as London equations, offering the first theoretical framework for the exotic electromagnetic properties of superconductors. It wasn't until another twenty-two years later that people finally constructed a microscopic theory for superconductivity, known as BCS theory.

In BCS theory, phonon exchange between electrons leads to the formation of Cooper pairs. However, later explorations revealed a vast class of superconducting materials whose transition temperature severely deviates from the prediction of the standard BCS theory, and theoretical investigations have suggested novel electron pairing mechanisms other than electron-phonon interaction. In particular, the pairing mechanism in iron-based superconductors is believed to be $s^{\pm}$ and d-wave pairing promoted by spin fluctuations [1]. In this report, we study the phase transition behaviors of samples $Ba(Fe_{1-x}Co_x)_2As_2$ belonging to such iron-based superconductors with different doping concentrations, and determine their doping rates according to their critical temperatures.

II. THEORETICAL FRAMEWORK

A. BCS Theory and Superconductivity

Nowadays, the BCS theory still remains the paradigmatic theory for superconductivity. Although the electron pairing mechanisms in non-BCS superconductors are different from phonon exchange, the electrons near the Fermi surface [2] which are responsible for superconductivity can nevertheless be described by the effective BCS Hamiltonian coupled to an electromagnetic field [3]:

$$\hat{H} = \int \mathrm{d}^d\boldsymbol{r}\; c_\sigma^\dagger(\boldsymbol{r})\left[\frac{1}{2m}(-\mathrm{i}\nabla - e\boldsymbol{A})^2 + e\phi - \mu\right]c_\sigma(\boldsymbol{r}) - g\int \mathrm{d}^d\boldsymbol{r}\; c_\uparrow^\dagger(\boldsymbol{r})c_\downarrow^\dagger(\boldsymbol{r})c_\downarrow(\boldsymbol{r})c_\uparrow(\boldsymbol{r}), \tag{1}$$

where $g > 0$, and is d the dimension. Introducing Hubbard-Stratonovich transformation induced by a complex scalar field Δ representing the energy gap in a superconductor, we obtain the partition function for the system:

$$Z = \int \mathcal{D}[\bar{\Delta}]\mathcal{D}[\Delta]\exp\left[\ln(\det\mathcal{G}^{-1}) - \frac{1}{g}\int \mathrm{d}\tau\mathrm{d}^d\boldsymbol{r}|\Delta|^2\right]. \tag{2}$$

Saddle point analysis reveals that its mean-field configuration Δ_0 satisfies the self-consistency equation

$$\frac{1}{g\nu} = \int_0^{\tau^{-1}} \mathrm{d}\xi \frac{\tanh\frac{\lambda(\xi)}{2T}}{\lambda(\xi)}, \tag{3}$$

where $\lambda_{\boldsymbol{p}} = \sqrt{\xi_{\boldsymbol{p}}^2 + |\Delta_0|^2}$, $\xi_{\boldsymbol{p}} \equiv \varepsilon_{\boldsymbol{p}} - \mu$, and ν is the state density near the Fermi level. Equation 3 have non-trivial solution for Δ_0 only for $T < T_c \propto \tau^{-1}e^{\frac{1}{g\nu}}$, and the mean-field energy gap below the critical temperature behaves like $\Delta_0 \propto \sqrt{T_c(T_c - T)}$.

The existence of an energy gap implies the ground state of the condensed Cooper pairs below the critical temperature can not be easily excited; hence, the energy dissipation in the system below the critical temperature is scarce. We also find that Δ is actually an order parameter associated with a second-order phase transition, so we can expand the effective action near the mean field

---

* Lab Report at Université Paris-Saclay.
† yiming.teng@universite-paris-saclay.fr
‡ derap-pena-mukti.sari@universite-paris-saclay.fr
§ xingyu.chen@universite-paris-saclay.fr

configuration and analyze it with the Ginzburg-Landau theory.

The effective action to the fourth order writes

$$S[\Delta,\bar{\Delta}]=\beta\int \mathrm{d}^d\boldsymbol{r}\left[\frac{r(T)}{2}\bar{\Delta}\Delta+\frac{c}{2}|\partial\Delta|^2+u(\Delta\bar{\Delta})^2\right], \quad (4)$$

whose $\sqrt{\frac{-r(T)}{4u}}\sim\sqrt{T(T-T_c)}$ for $T<T_c$. T_c turns to be a critical temperature for a spontaneous symmetry breaking, and the complex phase $\theta(\boldsymbol{r})$ of $\Delta(\boldsymbol{r})\equiv|\Delta(\boldsymbol{r})|e^{\mathrm{i}\theta(\boldsymbol{r})}$ corresponds to the Goldstone mode whose effective action is

$$S[\theta,A]=\int \mathrm{d}\tau\mathrm{d}^d\boldsymbol{r}\left[\nu(\partial_\tau\theta+\phi)^2+\frac{n_s}{m}(\nabla\theta-\boldsymbol{A})^2\right], \quad (5)$$

where n_s is the density of condensated Cooper pairs. Moreover, the electromagnetic field only couples to the Goldstone mode in a superconductor, and we can integrate out the Goldstone boson to derive the effective theory for the electromagnetic field in a superconductor:

$$S[\boldsymbol{A}]=\frac{\beta}{2}\sum_{\boldsymbol{q}}\left(\frac{n_s}{m}+q^2\right)\boldsymbol{A}_{\boldsymbol{q}}\cdot\boldsymbol{A}_{\boldsymbol{q}}. \quad (6)$$

The equation of motion for the vector potential from this action writes

$$\left(\frac{n_s}{m}-\nabla^2\right)\boldsymbol{A}(\boldsymbol{r})=0, \quad (7)$$

and it directly implies the first London equation describing the Meissner effect inside a superconductor:

$$\left(\frac{n_s}{m}-\nabla^2\right)\boldsymbol{B}(\boldsymbol{r})=0. \quad (8)$$

Meanwhile, the diamagnetic screening current density writes

$$\boldsymbol{j}(\boldsymbol{r})=\frac{\delta}{\delta\boldsymbol{A}(\boldsymbol{r})}\int \mathrm{d}^d\boldsymbol{r}\ \frac{n_s}{2m}\boldsymbol{A}^2=\frac{n_s}{m}\boldsymbol{A}(\boldsymbol{r}), \quad (9)$$

exemplifying the second London equation in the conventional phenomenological theory for superconductivity.

B. Cryogenics

The critical temperature for the superconductor phase transition in $\mathrm{Ba}(\mathrm{Fe}_{1-x}\mathrm{Co}_x)_2\mathrm{As}_2$ way below 77 K, and liquified helium is the primary refrigerant to reach this scale.

A closed-circuit helium gas cryostat is the core of our cryocooler system. The interior of the cryostat is partially vacuum ($\sim$ 1 mBar) to reduce thermal conduction by convection; at the same time, the cold head carrying the sample is subjected to a gold-plating process to provide its surface with high reflectivity, thereby suppressing radiative heat transfer and further enhancing thermal insulation between the system and the external environment.

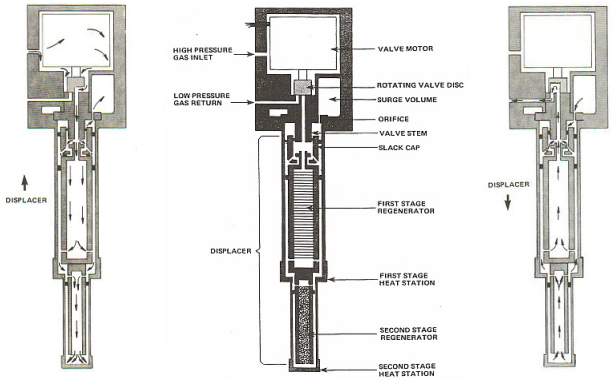

FIG. 1. Illustration of the cryostat structure.

The structure of the cryostat is depicted in Figure 1. Gifford-McMahon refrigeration cycle facilitates this instrument the ability to reach the helium temperature range [4]. At the start of each cycle, the displacer is at its lowest position, with the outlet valve closed and the inlet valve open, allowing high-pressure helium to fill the regenerator and upper space. As the displacer moves up, the gas is cooled isobarically while passing through the regenerator and fills the space below. With the displacer at its highest position, the inlet valve closes, the outlet valve opens, and the gas expands, producing refrigeration. The cycle completes as the displacer returns to the lowest position, warming the low-pressure gas and refilling the upper space.

Accurately measuring temperature variations is a necessity for this experiment. Calibrated DT-670 diodes are used for high-accuracy temperature measurements over a wide temperature range. Two diodes are mounted inside the cryostat: One is located adjacent to the sample platform and the other is attached to the second stage heat station. We suspect that these two thermosensors are calibrated for different temperature ranges, enabling the system to measure temperature from ambient temperature to the lowest cryogenic temperature. Besides, the two-sensor set-up allows for cross-verification of readings, hence improving the measurement confidence.

C. Four-Wire Resistance Measurement

Since we are conducting transport measurements on superconductors whose resistance is incredibly tiny, strategies for suppressing measured interference resistance originating from parts other than the sample must be adapted, and the four-wire measurement is the most common approach. In this set-up illustrated in Figure 2, a constant current source I provides the current flowing through the sample, and we will only measure the middle part of the sample (denoted as R). At the same time, the

contact resistance is abstracted to two resistors r_1, r_2 in series with the sample resistor R.

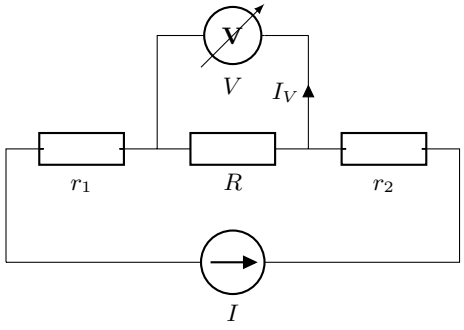

FIG. 2. Scheme for four-wire resistance measurement.

Denote the total resistance of the voltmeter and wires connected to it as R_V and the total contact resistance as $R_c \equiv r_1 + r_2$, we immediately have

$$V = (R_V + R_c)I_V = R(I - I_V), \tag{10}$$

hence, the current through the voltmeter writes

$$I_V = \frac{IR}{R_V + R}. \tag{11}$$

A reasonable estimation is that $R_V \sim 1\ \mathrm{M\Omega}$, thus

$$I_V \approx \frac{IR}{R_V} \ll I \tag{12}$$

and we can safely take $I_V \approx 0$. Eventually, we can regard the measurement on the voltmeter as faithfully representing the voltage on the tested resistor R, and Ohm's law for the ideal case is restored.

III. DATA ANALYSIS

A. General Comment

We measured the resistance-temperature relation ($R-T$ relation) for three samples, and the result is shown in Figure 3 and Figure 4. The cooling curve for Sample 2 is unavailable because of the malfunction of a connecting wire during the measurement. We have to use the three-wire method on this sample, and background resistance from contacts and wires isn't eliminated in this measurement.

According to our measurement, the resistances of Sample 1 and 3 in the ambient temperature are approximately $R_1 = 100\ \mathrm{m\Omega}$ and $R_3 = 130\ \mathrm{m\Omega}$. Assume these two samples have the same cross-sectional area S, then we can deduce the length for Sample 1 is $L_1 = 1.1$ mm, while the length of Sample 3 is $L_3 = 1.3$ mm, and S is estimated to be the mean value

$$S = \frac{\rho}{2}\left(\frac{L_1}{R_1} + \frac{L_3}{R_3}\right) \approx 3.57 \times 10^{-4}\ \mathrm{cm}^2. \tag{13}$$

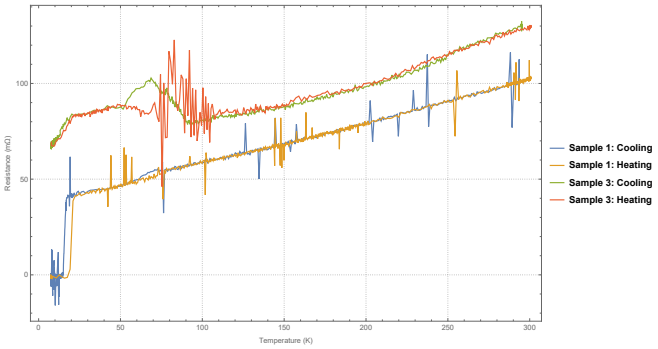

FIG. 3. $R-T$ relation of the Sample 1 and 3.

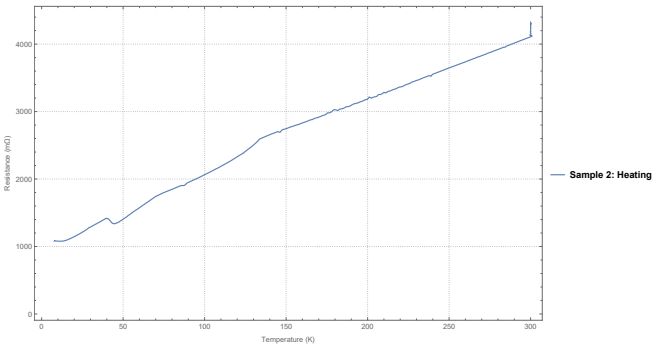

FIG. 4. $R-T$ relation of the Sample 2.

Given that the density of $BaFe_2As_2$ is 6.48 g/cm^3, the masses of Sample 1 and 3 are estimated to be $m_1 = 0.25$ mg, $m_3 = 0.3$ mg.

For all three materials, we observe the tendency that R decreases as T lowers for temperatures above the transition temperature. According to [5], both $BaFe_2As_2$ and $BaCo_2As_2$ are gapless. $Ba(Fe_{1-x}Co_x)_2As_2$ is a topological trivial material [6], hence at any doping rate, it will remain to be a conductor. Therefore, the temperature dependence at the high-temperature range can be explained by the classic Drude theory for metal conductivity: As T lowers, the carriers in the material are less thermally excited, and their frequency of colliding with impurities or lattice atoms are suppressed, resulting in less energy dissipation and lower resistance.

Focusing on the difference between the cooling curve and the heating curve for Sample 1 and 3 in Figure 3, we find the two cooling curves behave as their corresponding heating curves shifted to the left; hence the transition temperature indicated by the cooling curve is smaller than that reflected on the heating curve. This discrepancy can be explained by the fact that the cooling process requires a heat transfer from the sample to the heat station, and a temperature gradient exists between them. Therefore, the measured temperature in the cooling stage is slightly lower than the actual temperature of the sample. In contrast, the heat station and the sample are uniformly warmed up during heating, and we may regard their temperatures as the same. Therefore, data from the heating stage more faithfully represent our

samples' $R-T$ relations.

B. Transition Temperature

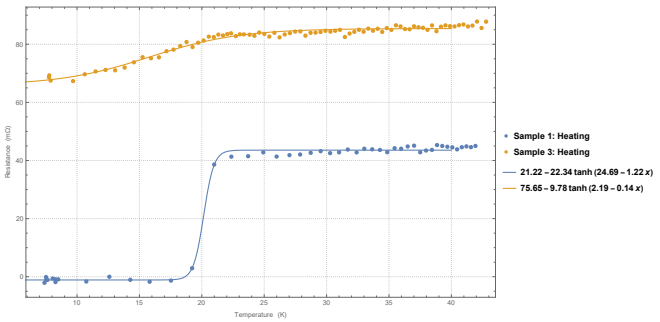

FIG. 5. Data from samples 1 and 3 near the transition point and the fitted curves.

Measurement on Sample 2 (Figure 4) shows no sign of resistance drop induced by superconductivity transition, and these data are discarded at this stage. For determining the critical temperatures of Sample 1 and 3, we focus on the region near the superconductivity transition (Figure 5) and notice:

- Before and after the superconductivity transition, the resistance is approximately constant.
- Superconductivity transition acts as a sudden resistance drop.

These two features suggest we use the tanh function for fitting the data in the vicinity of transition, and the result is also plotted in Figure 5. The position of the center of the tanh function can be identified as the transition temperature T_c, thereby

$$T_{c,1} = 20.15\ \text{K}, \quad T_{c,2} = 15.83\ \text{K}.$$

According to Figure 6, the estimation on the doping rate for these two samples is

$$x_1 = 0.056 \text{ or } 0.082, \quad x_2 = 0.048 \text{ or } 0.101.$$

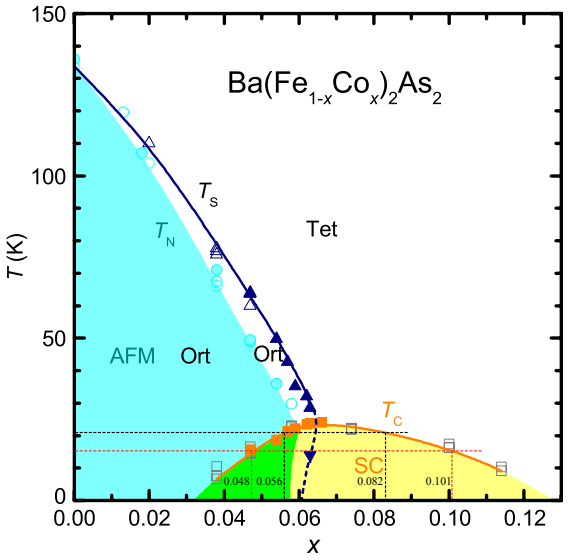

FIG. 6. Temperature-doping phase diagram of $Ba(Fe_{1-x}Co_x)_2As_2$ system [7].

IV. CONCLUSION

We analyzed the superconducting transition behaviors of $Ba(Fe_{1-x}Co_x)_2As_2$ samples under different doping concentrations using precision cryogenic techniques and resistance measurements. The measured resistance-temperature relation highlights the expected sudden resistance drop characteristic of the superconducting phase transition. For two of the samples, the critical temperatures were determined as $T_{c,1} = 20.15$ K,,$T_{c,2} = 15.83$ K; and their doping concentrations are constrained to $x_1 = 0.056$ or 0.082, $x_2 = 0.048$ or 0.101. Despite encountering limitations such as malfunctioning experimental apparatus and incomplete pathological data for one sample, this experiment enhanced our understanding of cryogenic technology and superconductivity.

Appendix A: Data Availability

All the raw data and the source code for the data analysis are available through the repository `https://github.com/Yiming-Teng/Superconductivity_data_analysis.git`.

[1] Sayak Ghosh, Matthias S. Ikeda, Anzumaan R. Chakraborty, Thanapat Worasaran, Florian Theuss, Luciano B. Peralta, P. M. Lozano, Jong-Woo Kim, Philip J. Ryan, Linda Ye, Aharon Kapitulnik, Steven A. Kivelson, B. J. Ramshaw, Rafael M. Fernandes, and Ian R. Fisher. Elastocaloric Evidence for a Multicomponent Superconductor Stabilized Within the Nematic State in $Ba(Fe_{1-x}Co_x)_2As_2$, 2024.

[2] To be more precise, they are electrons in a shell of width $\mathcal{O}(\tau^{-1})$, where τ is the relaxation time of the exchanged quasiparticle responsible for electrons pairing. Natural unit with $\hbar = c = 1$ is recognized.

[3] Alexander Altland and Ben Simons. *Condensed Matter Field Theory*. Cambridge University Press, 3rd edition,

September 2023.

[4] Steven W. Van Sciver. *Helium Cryogenics*. Springer New York, New York, NY, 2012.

[5] Anubhav Jain, Shyue Ping Ong, Geoffroy Hautier, Wei Chen, William Davidson Richards, Stephen Dacek, Shreyas Cholia, Dan Gunter, David Skinner, Gerbrand Ceder, and Kristin A. Persson. Commentary: The Materials Project: A materials genome approach to accelerating materials innovation. *APL Materials*, 1(1):011002, 07 2013.

[6] M. G. Vergniory, L. Elcoro, Claudia Felser, Nicolas Regnault, B. Andrei Bernevig, and Zhijun Wang. A Complete Catalogue of High-Quality Topological Materials. *Nature*, 566(7745):480–485, February 2019.

[7] S. Nandi, M. G. Kim, A. Kreyssig, R. M. Fernandes, D. K. Pratt, A. Thaler, N. Ni, S. L. Bud'ko, P. C. Canfield, J. Schmalian, R. J. McQueeney, and A. I. Goldman. Anomalous Suppression of the Orthorhombic Lattice Distortion in Superconducting $Ba(Fe_{1-x}Co_x)_2As_2$ Single Crystals. *Phys. Rev. Lett.*, 104:057006, Feb 2010.